4.1. Introduction

The swift advancement of emerging technologies has led to a notable upsurge in the need for electronic components. Concurrently, with the shrinking size of electronic devices, there has been a growing focus on ceramic capacitors possessing high dielectric constants, owing to their distinct attributes and it has been widely used in various applications, including telecommunication, consumer electronics, automotive electronics, medical devices, aerospace and defense applications [**1**–**3**]. $CaCu_3Ti_4O_{12}$ (CCTO), Complex cubic perovskite-like oxide, has received a lot of attention because of its unusually high dielectric constant (ε') (10^3–10^5) over a temperature range of 100 to 600 K with no structural phase transition and its apparent nonlinear current-voltage (current density-electric field, J-E) properties [**4**–**7**]. The high dielectric constant of the CCTO ceramic material has been a subject of interest to many researchers [**8**,**1**]. Several physical phenomena have been proposed to explain this phenomenon, but the most widely accepted model is the internal barrier layer capacitance (IBLC) model, which is an extrinsic mechanism [**9**–**11**]. According to the IBLC model, the CCTO ceramic is composed of two distinct components: n-type semiconducting grains and insulating grain boundaries. These components exhibit diverse electrical characteristics, indicating heterogeneity in their electrical properties. The emergence of a double Schottky potential barrier model at the junction of n-type semiconducting grains induces bending in the conduction band near the grain boundary region, resulting in a substantial increase in the dielectric constant [**12**,**13**]. The CCTO ceramic material also exhibits nonlinear current–voltage (I–V) properties. These nonlinear properties result from the double Schottky potential barrier models formed at the interface between the n-type semiconducting grains [**14**,**15**]. Because of its pronounced nonlinear attributes, CCTO ceramics find applicability not just in

capacitors but also in varistor devices for potential uses. $Bi_{2/3}Cu_3Ti_4O_{12}$ (BCTO) is one of the few currently known isostructural CCTO-like oxides [**16**]. BCTO has also been synthesized by various processes that affect the dielectric and electrical characteristics. Yang et al. used the solid-state method to create a series of high-density BCTO and obtained a high dielectric permittivity of $\approx 3.39 \times 10^5$ at 1 kHz [**17**]. In a $Bi_{2/3}Cu_3Ti_4O_{12}$ /$Bi_3LaTi_3O_{12}$ nanocomposite, P. Gautam and co-workers observed a dielectric constant value of 13.94×10^3 and a dielectric loss of ≈2.4 at 503 K [**18**]. Pooja et al. investigated the dielectric characteristics of BCTO manufactured through the semi-wet approach in the frequency range 100 Hz–1 MHz and found a high dielectric constant ($\varepsilon' \approx 8 \times 10^3$), while the minimum value of the dielectric loss is ≈9 at 1 kHz [**19**]. Because of the substantial tangent loss (tan δ) of BCTO, they are inappropriate for capacitor applications. As a result, the lowering of tan value is a significant and urgent topic that requires consideration. Among the undertaking experiences is one in which doping is an efficient means of reducing tan δ value. However, only limited work has been done recently in BCTO ceramics based on partial substitution of Bi, Cu, or Ti ions to reduce the tan δ such as Dy^{3+} doped at Bi^{3+} site,[**20**] Zn^{2+} doped at Cu^{2+} site,[**21**] and Mg^{2+} doped at Cu^{2+} site [**22**].

Until now, no documentation exists regarding the dielectric properties of BCTO ceramics doped with Sm^{3+}. The introduction of Sm^{3+} into the BCTO ceramics induces modifications in their microstructure, solves the Bi volatility problem, and improves sinterability and enhance the lattice distortion. Consequently, the primary objective of this study is to explore the impact of Sm^{3+} dopant ions on the microstructure, dielectric characteristics, and electrical behavior of BCTO ceramics.

4.2. Experimental

$Bi_{(2/3)-x}Sm_xCu_3Ti_4O_{12}$ (BSCTO x = 0.05, 0.10, and 0.20) was synthesized using an easy-handling semi-wet method in this study. As a raw material, $Bi(NO_3)_3.5H_2O$ (99% purity) copper acetate $Cu(CH_3COO)_2$. H_2O (99% purity), titanium oxide TiO_2 (98.5% purity), and Sm_2O_3 (99.99% purity) were used and citric acid was used as the chelating agent. The raw materials were thoroughly mixed by stirring them in water for 20 h to achieve homogeneity. The gel was created using this method [**56**]. The resultant gel was then heated in air for 30 min at 373 K to evaporate all liquid from the samples, and the precursors were calcined for 6 h at 1073 K. The powders that had undergone calcination were subsequently crushed and compacted into pellets with a diameter of 1 mm, utilizing a pressure of ≈5 tons. Ultimately, these pellets were sintered in an air environment at a temperature of 1173 K for 8 h. The sintered $Bi_{(2/3)-x}Sm_xCu_3Ti_4O_{12}$ ceramics with x = 0.05, 0.1, and 0.2 were abbreviated as BSCTO-0.05, BSCTO-0.1, and BSCTO-0.2 samples, respectively.

The phase composition and crystal structure of sintered BSCTO ceramics were investigated using X-ray diffractometry (Rigaku miniflex 600, Japan) with Cu Kα radiation in a 2θ range of 20–80 °. SEM (ZEISS; model EVO18 research, Germany) and energy-dispersive X-ray spectrometry (EDS) (Oxford instrument, USA) was employed to characterize the microstructure and elemental distributions of the BSCTO ceramics. X-ray photoelectron spectroscopy (XPS) is used to investigate the chemical valence states of ceramic components. A high-performance frequency LCR meter (E4980A/AL, Keysight,) was used to evaluate the dielectric characteristics and complex impedance with applied voltages in the frequency and temperature ranges of 20 Hz to 2 MHz and 303 to 503 K, respectively.

4.3. Results and discussion

4.3.1. Microstructural studies

Figure **4.1 (**a) displays the XRD (X-ray diffraction) patterns of $Bi_{(2/3)-x}Sm_xCu_3Ti_4O_{12}$ (BSCTO x = 0.05, 0.10, and 0.20) samples that were sintered at 1173 K for 8 hours. The XRD patterns, shown in Figure **4.1 (**a), indicate the presence of diffraction peaks that are characteristic of the BCTO (Calcium Copper Titanate) phase. For all samples, the diffraction peaks are indexed to a cubic perovskite-related structure as confirmed by comparing them to the reference data in the standard powder diffraction file database (JCPDS File No. 75-2188) [**23**]. The XRD analysis indicates that the ceramics are composed entirely of the BCTO phase, confirming the successful integration of Sm^{3+} ions into the lattice structure of BCTO. This inclusion of Sm^{3+} dopants is evident in the creation of a pure BCTO phase with the space group Im-3 for all the ceramic samples. The enlargement of the diffraction pattern view of 2θ from 31.8º to 36.7º, as shown in Figure **1** (b), indicates that the positions of the diffraction peaks shift towards higher 2θ as the Sm^{3+} content increases. This observed shift in the diffraction peaks can be attributed to lattice contraction caused by the partial substitution of Bi^{3+} cations with cation Sm^{3+} [**25**]. Debye-Scherrer method was used to determine the average crystallite sizes (D) of all samples based on the X-ray line broadening of the peaks [**25**].

$$D = \frac{k\lambda}{\beta cos\theta} \qquad 4.1$$

where β represents the Full Width at Half Maximum (FWHM) of the intensity (measured in arbitrary units) versus the 2θ pattern. The symbol λ stands for the wavelength of Cu Kα radiation, which has a value of 0.15406 nm. Meanwhile, θ denotes the angle of Bragg's diffraction. The parameter D corresponds to the size of the crystallite, and the value of constant k relies on the nature of the crystallite's shape. Specifically, for spherical particles, k

is set to 0.89. The computed D values for BSCTO ceramics exhibit an initial increase followed by a subsequent decline as the compositions vary, as depicted in Table **4.1**. Since the Debye-Scherrer method does not account for the strain effect when determining crystallite size, the Williamson-Hall (W-H) analytical approach [**26**, **27**] has been introduced. This approach allows for the inclusion of micro-strain (ε) for all particles and provides a more accurate value for both crystallite size and micro-strain. Equation **4.2** is utilized in this approach to estimate these properties and gain additional insights into the structural characteristics:

$$\beta \quad cos\theta = \left(\frac{k\lambda}{D}\right) + 4\varepsilon \quad sin\theta \qquad 4.2$$

Where ε denotes the micro strain in the crystal.

Figure **4.2** illustrates how the linear fit can be used to derive the value of "β cosθ" vs. "4 sinθ" and micro-strain. All samples show a positive slope, which indicates the presence of tensile strain in the as-prepared sample structures. Table **4.1** also includes the microstructural parameters determined by the Williamson-Hall plot. The data presented in Table **4.1** indicates a noticeable pattern in the calculated crystallite size using both the Debye-Scherrer and Williamson-Hall plot methods. Initially, there is an increase in size, followed by a subsequent decrease, and micro-strain in the BSCTO ceramics also follow Opposite trends as the concentration rises. This demonstrates that the emergence of lattice strain within the crystal lattice due to a disparity in ionic sizes between bismuth and samarium leads to a state of localized structural irregularity, consequently diminishing the size of the crystalline entities [**29**].

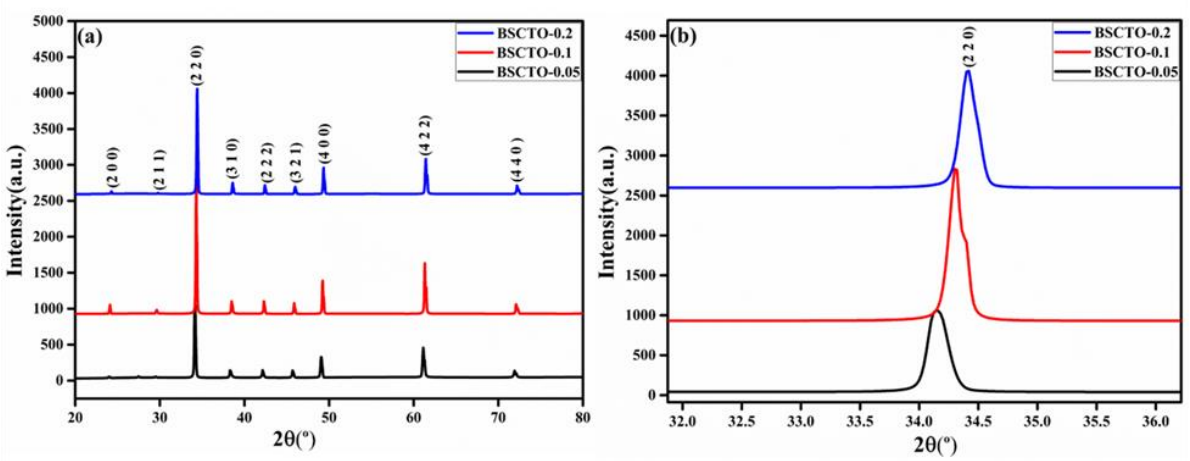

Fig. 4.1 (a) XRD Pattern and (b) Enlarges view of most instance peak of sintered BSCTO ceramics

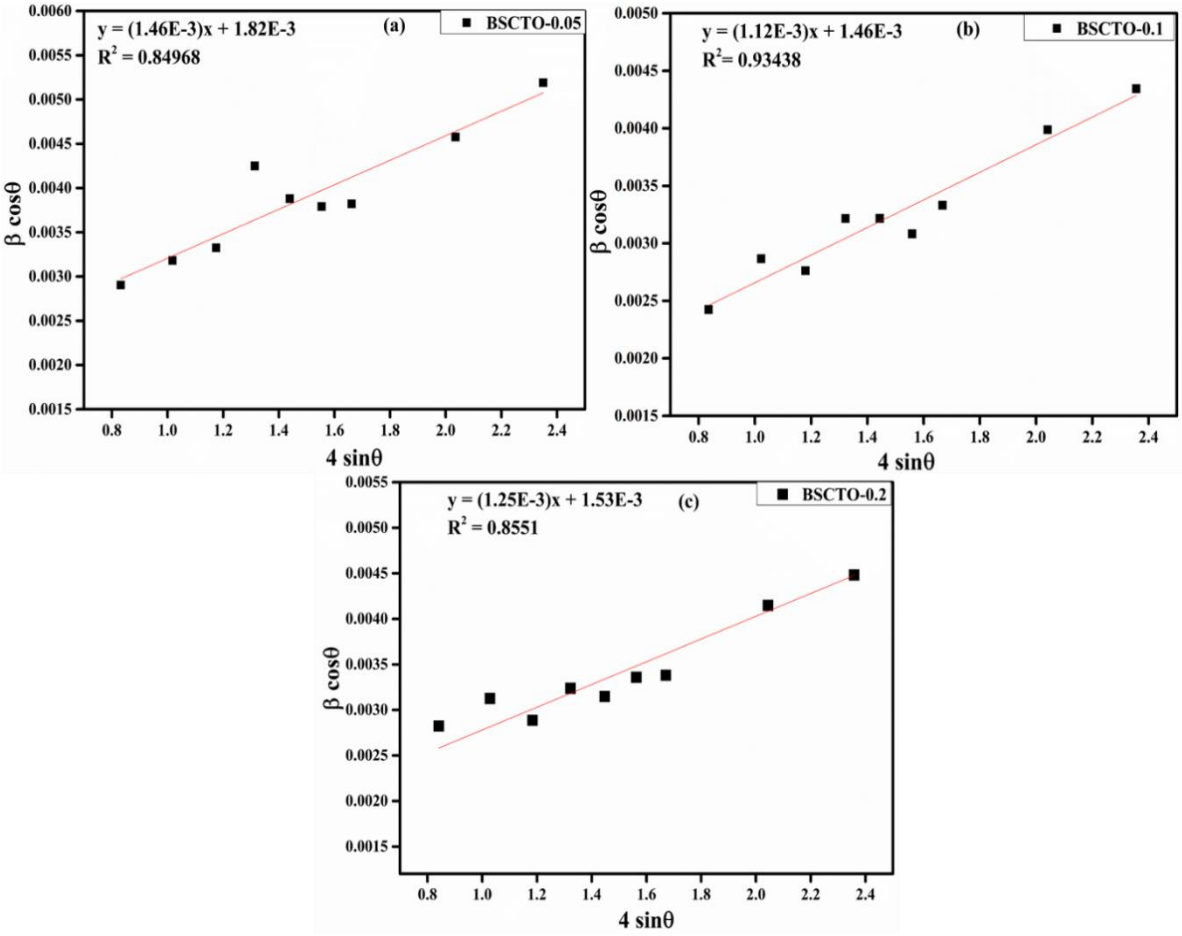

Fig. 4.2 William-Hall Plot of all three Sintered BSCTO ceramics

Table 4.1 The comparison of crystallite size by Debye-Scherrer Method and Williamson-Hall Plot of BSCTO ceramics

	Debye-Scherrer Method	Williamson-Hall Plot	
	Crystallite Size (nm)	Crystal Strain (10^{-3})	Crystallite Size (nm)
BSCTO-0.05	62.13	1.46	76.15
BSCTO-0.1	81.54	1.12	94.93
BSCTO-0.2	69.81	1.25	90.89

In addition, to investigate the effect of Sm3+ dopant on the crystal structure, Rietveld analysis of the X-ray diffraction data of $Bi_{(2/3)-x}Sm_xCu_3Ti_4O_{12}$ (BSCTO x = 0.05, 0.10, and 0.20) ceramics were performed using "FullProf" software as shown in Figure **4.3** (a-c). The Pseudo-Voigt function was used to simulate the Bragg peaks, and linear interpolation between selected background points was used to estimate the background. The space group, lattice parameter, atomic locations (x, y, z), atomic site occupancies, and full-width half parameters (u, v, w) were all refined until a good fit was achieved. Table **4.2** shows the refinement results, which include unit cell parameters, atomic position co-ordinates, profile R-factors, and Goodness of fit (GOF). The experimental XRD patterns were well matched, as evidenced by low GOF values (2< for all samples) and acceptable R_{exp}, R_{wp}, and R_p values. The Rietveld analysis yielded the cubic phase lattice parameter of BSCTO ceramics, which was compared to the crystallographic structure of pristine BCTO [JCPDS 75-2188]. The lattice parameter of Sm doped BCTO samples obtained from the Rietveld analysis, as reported in Table **4.2** decreases with a rise in dopant concentration which is thought to be caused by the presence of smaller dopant ions than the equivalent host ions in pristine BCTO. Figure **4.3 (d)** is a Cubic crystal structure representation of the Sm doped compound. BCTO is a derivative of $ACu_3Ti_4O_{12}$ ($A = Bi^{3+}$) with body centered Cubic crystal structure. Its crystal structure is

comprised mainly of two building block units, namely, CuO_4 square planes containing Cu^{2+} ions share corners with the TiO_6 octahedra containing Ti^{4+} ions respectively. It is the TiO_6 octahedra which plays a significant role in structure distortion.

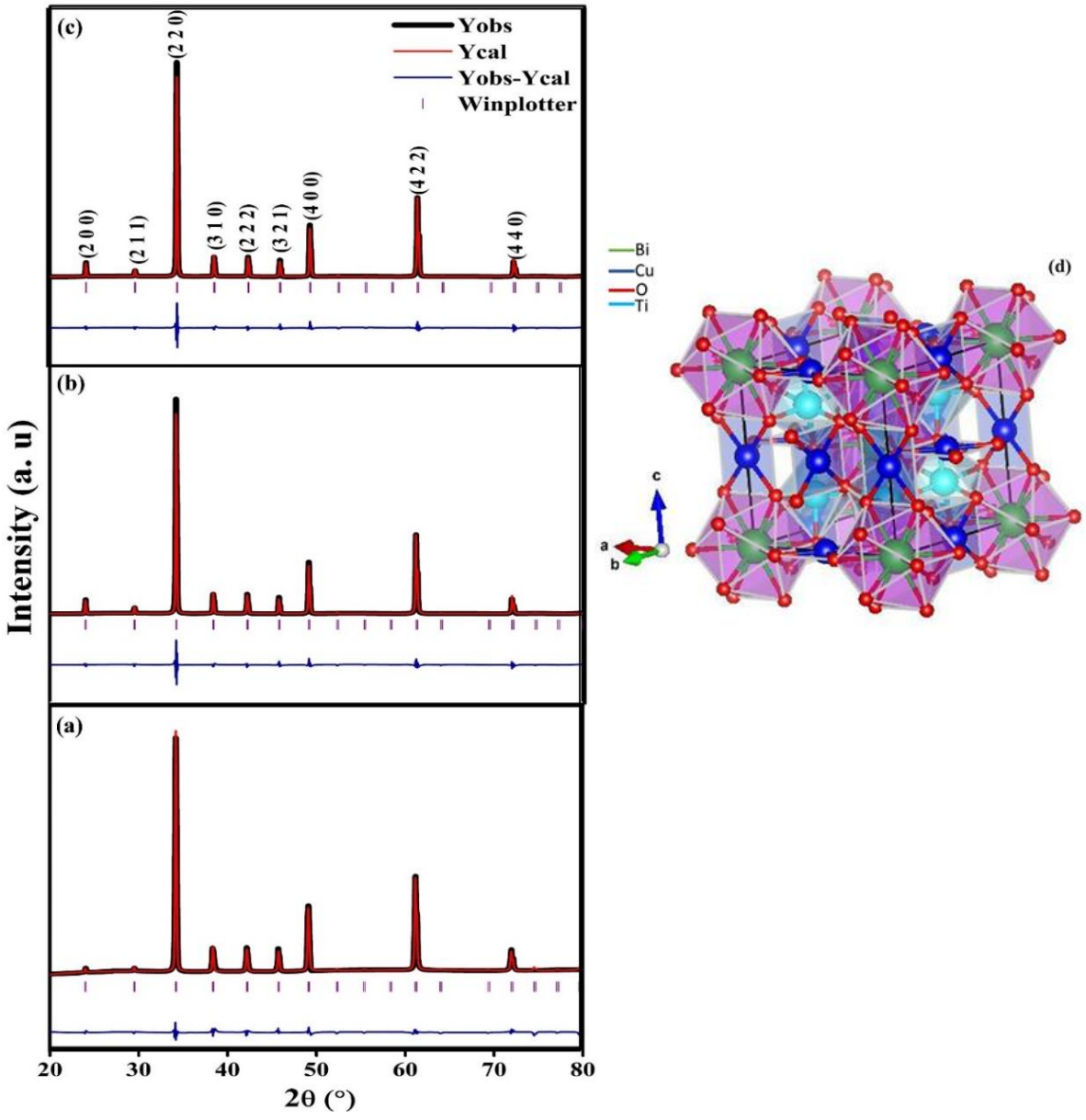

Fig. 4.3 (a-c) Rietveld analysis of $Bi_{(2/3)-x}Sm_xCu_3Ti_4O_{12}$ (BSCTO x = 0.05, 0.10, and 0.20) ceramics and (d) Crystal representation of BSCTO-0.2 ceramic.

Table 4.2 Chi-square(χ^2), space group, Lattice parameters, Vcell, FWHM parameters, Conventional Rietveld R-factors, Bragg's- R factor, RF-factor and structural parameter of BSCTO ceramic with the concentration of 0.05, 0.10, and 0.20, respectively.

Refinement Condition of XRD pattern: wavelength = 1.54 Å and N. of cycle used in refinement = 0.02 °/sec

Observed parameters	BSCTO-0.05	BSCTO-0.1	BSCTO-0.2
χ^2	0.174	0.144	0.251
space group	Im-3	Im-3	Im-3
Lattice parameters (Å)	a = b = c=7.419394	a = b = c= 7.411491	a = b = c=7.409999
V_{cell} (Å^3)	408.1702307	407.114674	406.868856
FWHM parameters	U= 0.021669 V= - 0.001283 W= 0.023661	U= 0.018111 V= -0.005231 W= 0.012181	U= 0.143383 V= - 0.112520 W= 0.037544
Conventional Rietveld R-factors			
R_p (%)	18.2	15.8	29.0
R_{wp} (%)	15.6	12.1	17.6
R_{exp} (%)	37.46	31.79	35.21
Bragg' R-factor (%)	3.38	3.961	1.918
RF-factor (%)	5.78	5.673	2.564

BSCTO-0.05	X	Y	Y	Occupancy	Site	Symmetry
Bi1	0.00000	0.00000	0.00000	0.03159	2a	m-3.
Cu1	0.00000	0.50000	0.50000	0.13953	6b	mmm . .
Ti1	0.25000	0.25000	0.25000	0.20913	8c	.-3.
O1	0.29520	0.18107	0.00000	0.70283	24g	m..
BSCTO-0.1						
Bi1	0.00000	0.00000	0.00000	0.06209	2a	m-3.
Cu1	0.00000	0.50000	0.50000	0.24667	6b	mmm . .
Ti1	0.25000	0.25000	0.25000	0.29964	8c	.-3.
O1	0.29611	0.18026	0.00000	1.48667	24g	
BSCTO-0.2						
Bi1	0.00000	0.00000	0.00000	0.01500	2a	m-3.
Cu1	0.00000	0.50000	0.50000	0.10662	6b	mmm . .
Ti1	0.25000	0.25000	0.25000	0.14559	8c	.-3.
O1	0.30481	0.18058	0.00000	0.50128	24g	m..

To extract information regarding the morphological aspects of synthesized samples was done by the field emission scanning electron microscopy (SEM) technique. Morphology of the sintered $Bi_{(2/3)-x}Sm_xCu_3Ti_4O_{12}$(BSCTO x = 0.05, 0.10, and 0.20) samples are shown in Figure **4.4 (**a-c). All the synthesized BSCTO samples show a drastic variation in the microstructure as observed in the SEM images. The average grain sizes of sintered BSCTO samples are approximately 1.029 μm, 0.832 μm, and 0.753 μm, respectively. This suggests that higher concentrations of Sm-doping in BCTO result in the suppression of grain growth. This decrease in grain size on increasing the dopant concentration is attributed to the suppression of oxygen vacancy and increase in deformation in the crystal structure, and the changes with ionic mobility during the sintering process [**28**,**29**]. EDS analysis was conducted to provide additional insights into the microstructure. The EDS spectrum displayed in Figure **4.4 (**d-f) illustrates the presence of all constituent elements (Bi, Sm, Cu, Ti, and O) within the BSCTO ceramics. The Inset table of EDS figures presents the weight (Wt%) and atomic percentages (At%) of these elements detected in the ceramics.

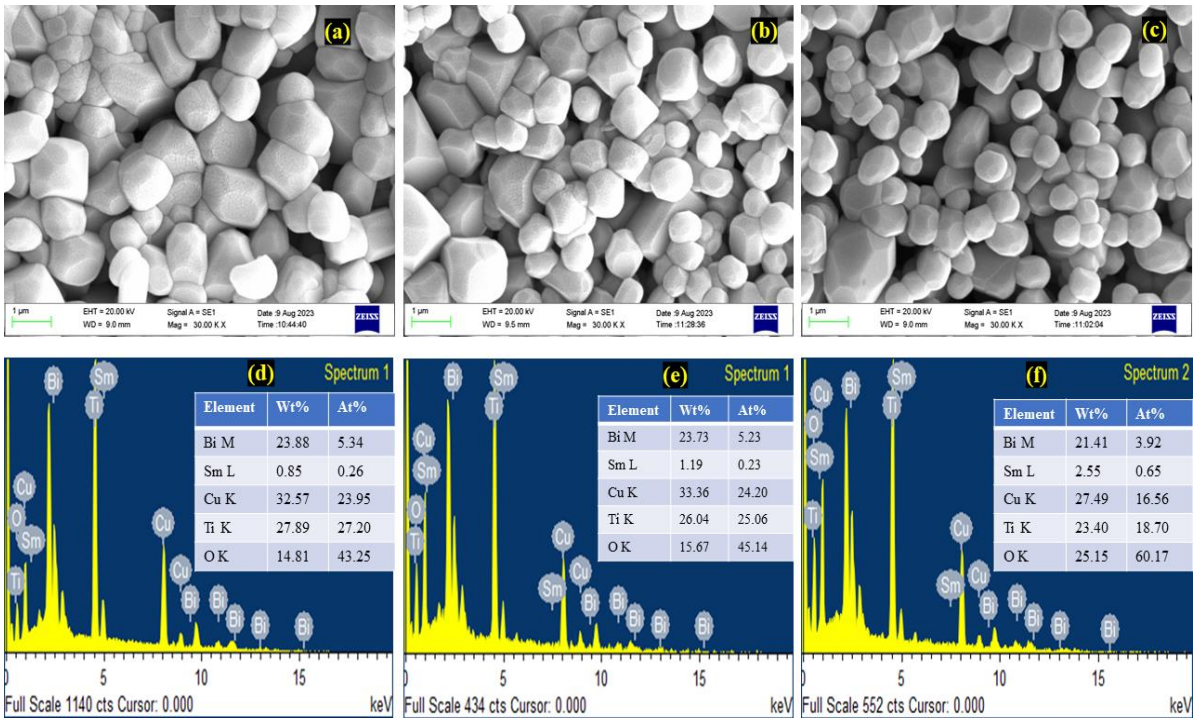

Fig. 4.4 (a-c) SEM micrograph and (d-f) EDS analysis results of BSCTO-0.05, BSCTO-0.1 and BSCTO-0.2 respectively

Figure **4.5 (**a–c) displays 3D-AFM topographic images of BSCTO ceramics at different concentrations (x = 0.05, 0.10, and 0.20). Each sample was scanned over an area of 30 × 30 μm². The results indicate a reduction in surface root mean square roughness (Rrms) as the proportion of Sm^{3+} ions increase, with values of 0.307 μm, 0.263 μm, and 0.194 μm for x = 0.05, 0.10, and 0.20, respectively. In Figure **4.5 (**d-f), the histogram presents the grain sizes of BSCTO samples. An increase in Sm-doping corresponds to the formation of smaller grain sizes across the surface. The grain sizes determined from the AFM micrographs decrease as the dopant concentration rises, consistent with the trends observed in grain sizes from SEM images. Notably, the grain sizes observed through SEM/AFM are larger compared to the crystallite sizes calculated from XRD data. This divergence arises because XRD provides an average crystallite size, while SEM/AFM reveals grains that result from the aggregation of multiple crystallites [**30**, **31**].

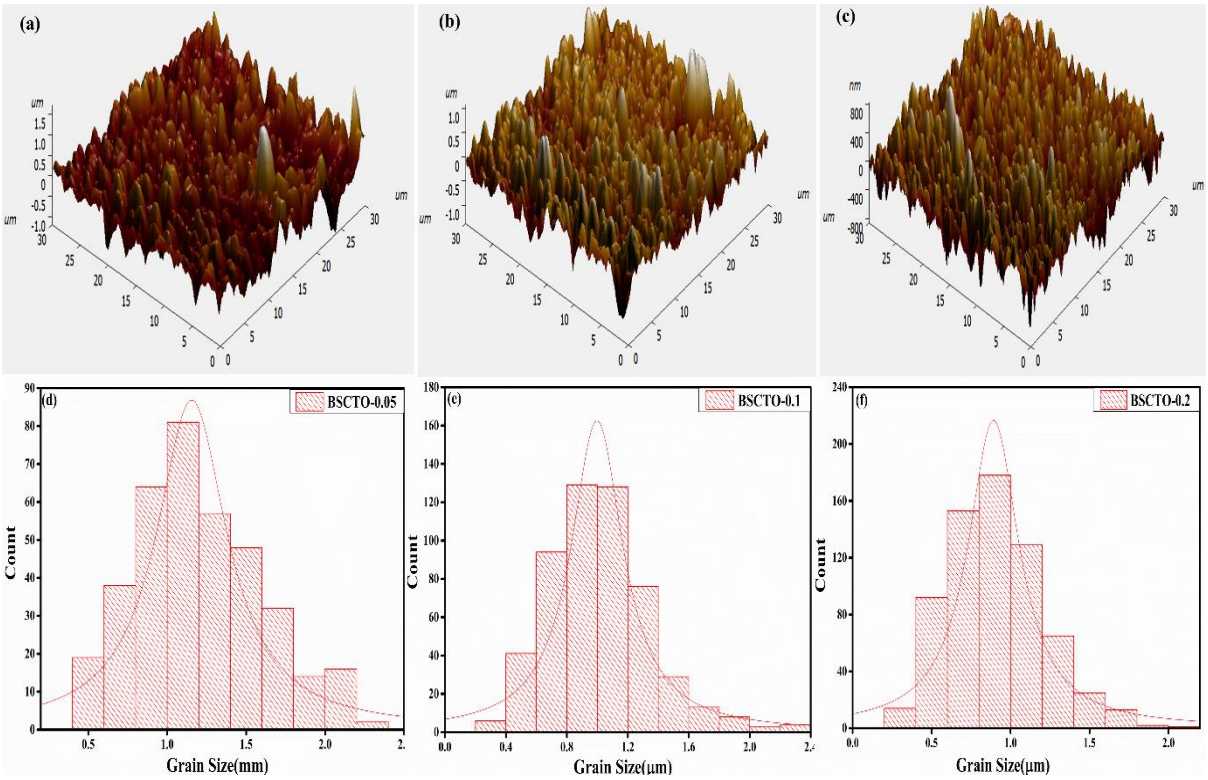

Fig. 4.5 (a-c) 3D AFM image and (d-f) Grain size distribution curve of BSCTO-0.05, BSCTO-0.1, and BSCTO-0.2 respectively

In order to identify the electronic state of the Bi, Sm, Cu, Ti, and O elements, thorough XPS analysis was performed on the BSCTO-0.2 sample in a binding energy range of 0-1200 eV, and the resulting spectra of the different elements are shown in Figure **4.6 (**b-f). The survey spectra given in Figure **4.6 (**a) demonstrate the obvious peak signals of all the requisite system constituents. Figure **4.6 (**b) reveals a Bi 4f doublet with two peaks at 158.8 eV ($4f_{7/2}$) and 164.1 eV ($4f_{5/2}$), confirming the dominating 3+ oxidation state of Bi in BSCTO-0.2 ceramic [**32**]. The slight shift of Bi 4f peaks towards higher binding energy shows Sm^{3+} ion substitution at the Bi^{3+} site in the BCTO lattice**.** The chemical shifting Bi $4f_{7/2}$ and Bi $4f_{5/2}$ peaks arises due to variation in the electro-negativity of Bi, Sm, Cu, Ti, and O elements. The Sm 3d XPS spectrum has two components that are connected to Sm^{3+} and Sm^{2+} [**33**,**34**]. The

primary peaks for Sm $3d_{5/2}$ and Sm $3d_{3/2}$ are located at 1082.4 and 1107.8 eV, respectively, and are associated with the Sm^{3+} components. Furthermore, as seen in Figure **4.6** (c), the conspicuous peak centered at 1100 eV was associated with the divalent state of Sm. The XPS Cu 2p spectra are displayed in Figure **4.6** (d). The binding energy peaks of Cu 2p spectra at 935.8 eV($2p_{3/2}$) and 954.7 eV($2p_{1/2}$) in BDCTO-0.2 ceramic support the existence of the + 2 oxidation state of Cu [**35**]. The XPS core spectra of two Ti 2p peaks at 464.21 and 458.42 eV, which correspond to Ti $2p_{1/2}$ and Ti $2p_{3/2}$, are shown in Figure **4.6** (e). Deconvoluting the $2p_{3/2}$ peak reveals two peaks, one at 458.17 eV and the other at 459.49 eV, corresponding to tetravalent and trivalent oxidation states of titanium, respectively. This revealed that Ti^{3+}/Ti^{4+} coexisted in the lattice [**34**]. The peak at 464.01 eV and 456.34 eV for $2p_{1/2}$ is also ascribed to the +3 and +4-oxidation state of titanium. The presence of low valency ions is caused by the formation of imperfection/defect or defect pairs in the lattice, which aids in charge separation or maintains charge compensation. Figure **4.6** (f) shows the O 1s profile of BSCTO-0.2 ceramics. It was found that the O 1s consists of three components which are a main peak at 529.55 eV and a higher-energy peak at 530.77 eV, which corresponds to the lattice oxygen and the presence of oxygen vacancies. A relatively weaker peak around 532.3 eV is identified as the oxygen in the OH groups or absorption of water moisture, which is adsorbed on the surface of the particle [**36**].

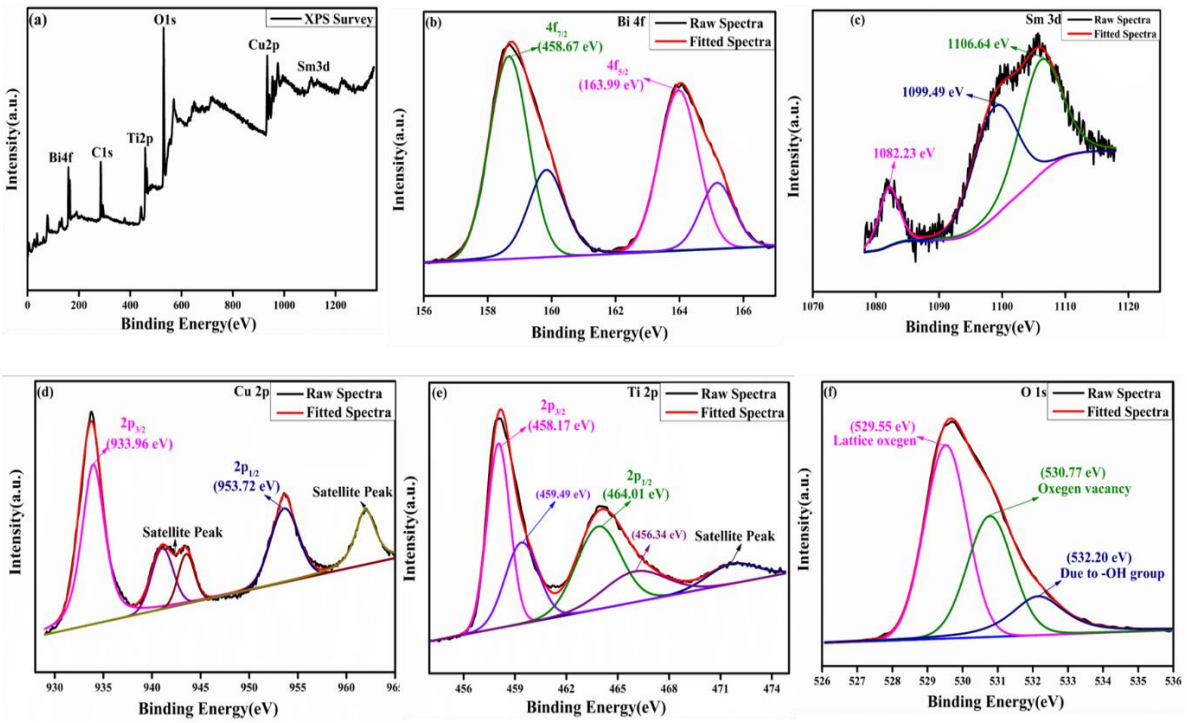

Fig. 4.6 XPS (a) Survey Spectrum, (b) Bi, **(c)** Sm, (d) Cu**,** (e) Ti, (f) O, respectively of BSCTO-0.2 ceramic

4.3.2. Dielectric Studies

Figure **4.7** (a, b) depicts the dielectric constant (ε′) and dielectric loss (tan δ) of the BSCTO sample change with temperature at 1 kHz for various compositions (x = 0.05, 0.10, and 0.20). It can be seen that the dielectric constant and dielectric loss of all synthesized samples decreases with an increase in samarium concentration. This outcome aligns with findings in the existing literature.[**37**] Furthermore, it is noticeable that the dielectric constant and dielectric loss remain relatively stable until reaching a temperature of 400 K, beyond which they start to rise with increasing temperature. This observed behavior was reported previously by Uniyal et al., who attributed this effect to the influence of space charge polarization and the presence of oxygen vacancies at elevated temperatures.[**38**] The lower values of ε′ and tan δ for BSCTO ceramic with higher concentration at 1 kHz and 303 K obtained from the plots are found to be 80 and 0.04, respectively.

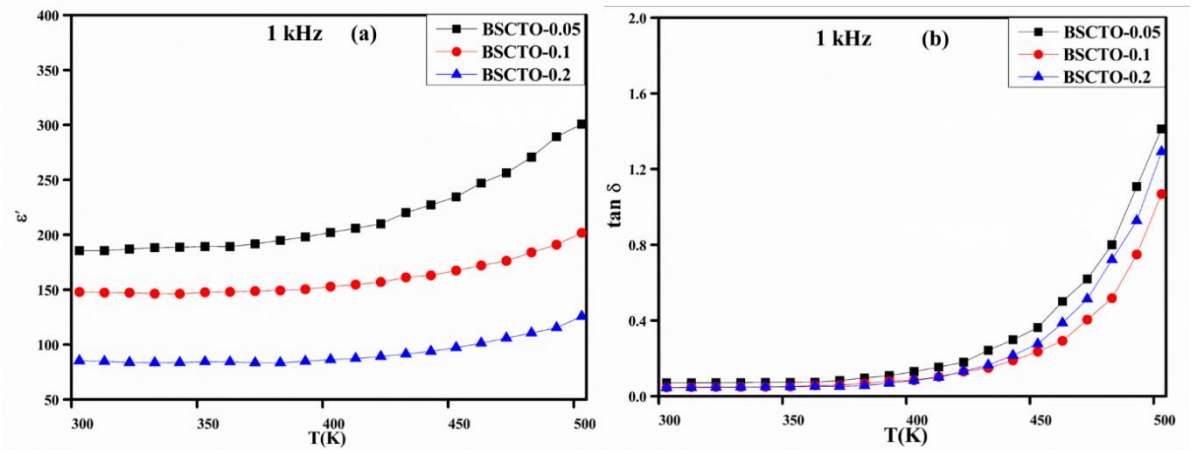

Fig. 4.7 Variation of (a) dielectric constant and (b) dielectric loss with temperature at 1 kHz for $Bi_{(2/3)-x}Sm_xCu_3Ti_4O_{12}$ (x = 0.05, 0.10, and 0.20)

The fluctuation of the dielectric constant(ε′) of synthesized and sintered BSCTO ceramics with various concentrations as a function of different frequencies and at room temperature is shown in Figure **4.8** (a). It clearly from the figure that the ε′ decreases as the concentration of Sm^{3+} doping ions increases. The reduction in ε′ is linked to the diminishing grain size. This observation in Sm-doped BCTO ceramics corresponds to findings documented in existing literature concerning various other ceramic materials. It can be seen that Sm^{3+} doping in BCTO has a considerable impact on the permittivity of the BCTO ceramic, resulting in a decrease in permittivity. The finding is easily explained by the internal barrier layer capacitor (IBLC) hypothesis which suggests that the microstructure plays a crucial role in determining the dielectric constant of the ceramic. The dielectric permittivity of the samples depends on the conductivity of semiconducting grains which is caused by the densification and sample of porous grains requires more energy for electron hopping and also wastes more heat. As a result, the dielectric constant of the sample will be reduced [**39**–**41**]. It is determined using the subsequent expression:

$$\varepsilon' = \frac{\varepsilon_{gb}}{t_{gb}} G \qquad 4.3$$

where G, ε_{gb}, and t_{gb} are the average grain size, grain boundary thickness, and effective dielectric constant respectively. Equation **4.3** reveals that the ϵ' for CCTO ceramics decreases as the grain size decreases. The values of ε′ at 1 kHz for samples (x = 0.05, 0.10, and 0.20) were found to be 289, 145, and 82, respectively. it is also noted that the dielectric constant and dielectric loss (tan δ) exhibit a decline as the frequency increases. This trend is a common characteristic observed in polar dielectric materials, regardless of the composition of the samples. The decline in dielectric constant as frequency rises is a general; trend and can be elucidated by the dipolar relaxation phenomena resulting from interfacial polarization of the Maxwell–Wagner type [**44**]. The polarization of a dielectric material is the sum of the contributions of several types of polarizations, such as dipolar, electronic, ionic, and interfacial polarizations with varying relaxation times [**45**]. At lower frequencies, all polarization types readily respond to electric field variations, resulting in a higher observed dielectric constant. However, at higher frequencies, individual polarization contributions begin to relax, and interfacial dipoles have limited time to align with the alternating field [**46**]. Consequently, the overall material polarization decreases, leading to a reduction in the dielectric constant as frequency increases. Figure **4.8** (b) depicts the frequency dependence of tangent loss (tan δ) at 303 K for the BSCTO samples. The figure indicates a significant reduction in the tan δ values of Sm-doped BCTO ceramic compared to the undoped BCTO ceramic across the frequency range. This reduction is attributed to the introduction of Sm^{3+} through doping, which is potentially linked to the enhancement of both intrinsic and/or extrinsic characteristics at the grain boundary [**47**-**49**]. The dielectric loss value at 1 kHz was

found to be 0.37, 0.08, and 0.04 for the x = 0.05, x = 0.10, and x = 0.20 Sm-doped of BCTO ceramics, respectively.

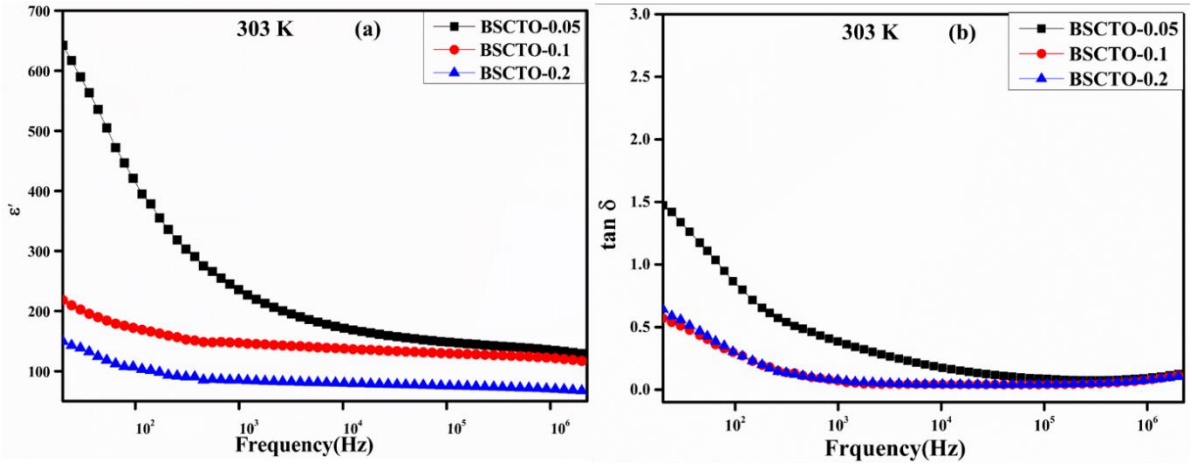

Fig. 4.8. (a) Dielectric constant and (b) tan δ of $Bi_{(2/3)-x}Sm_xCu_3Ti_4O_{12}$ (x = 0.05, 0.10, and 0.20) over a wide range of frequency (20 Hz-10 MHz).

Impedance spectroscopy is a prominent technique for the determination of the grain boundary and grain responses in order to understand the fundamental mechanisms underlying the dielectric and electrical results. A series circuit of two parallel resistor-capacitor (RC) circuits is commonly recognized to demonstrate the electrical heterogeneity of BCTO ceramics, in accordance with the IBLC model. Figure **4.9** illustrates the Complex impedance plot (Z″ versus Z′) depicting the behavior of BSCTO ceramics across various temperatures as well as ambient temperature within the frequency range of 20 Hz–10 MHz. It clears from Figure **4.9** (a–c) that the semicircle diameters diminish as the temperature rises, resulting in a decrease in the overall material resistivity. This reduction indicates the emergence of a thermally activated conduction mechanism within both the grains (R_g) and at the grain boundaries (R_{gb}) [**47**]. In Figure **4.9** (d), a partial or incomplete semicircular arc is found for all concentrations of Sm-doped BCTO ceramics due to the contribution of the bulk R_g and R_{gb} effects. Additionally, a meticulous examination of the high frequency region indicates minimal

alteration in grain resistivity due to Sm-doping, as illustrated in the inset of Figure **4.9** (d). Furthermore, the grain boundary resistance values extracted from Figure **4.9** (d) are increased approximately in the order of magnitude from 1.23×10^7 Ω, 1.52×10^7 Ω, and 2.51×10^7 Ω, respectively, as the Sm^{3+} concentrations rise. Higher R_{gb} in ceramics always results in lower tan δ at low frequencies. R_g Values are almost very low when compared to R_{gb}, as indicated in the inset of Figure **4.9** (d). The significant difference arises from the substantial variation in electrical properties between individual grains and the grain boundaries within ceramic samples. which is consistent with the IBLC model [**48**].

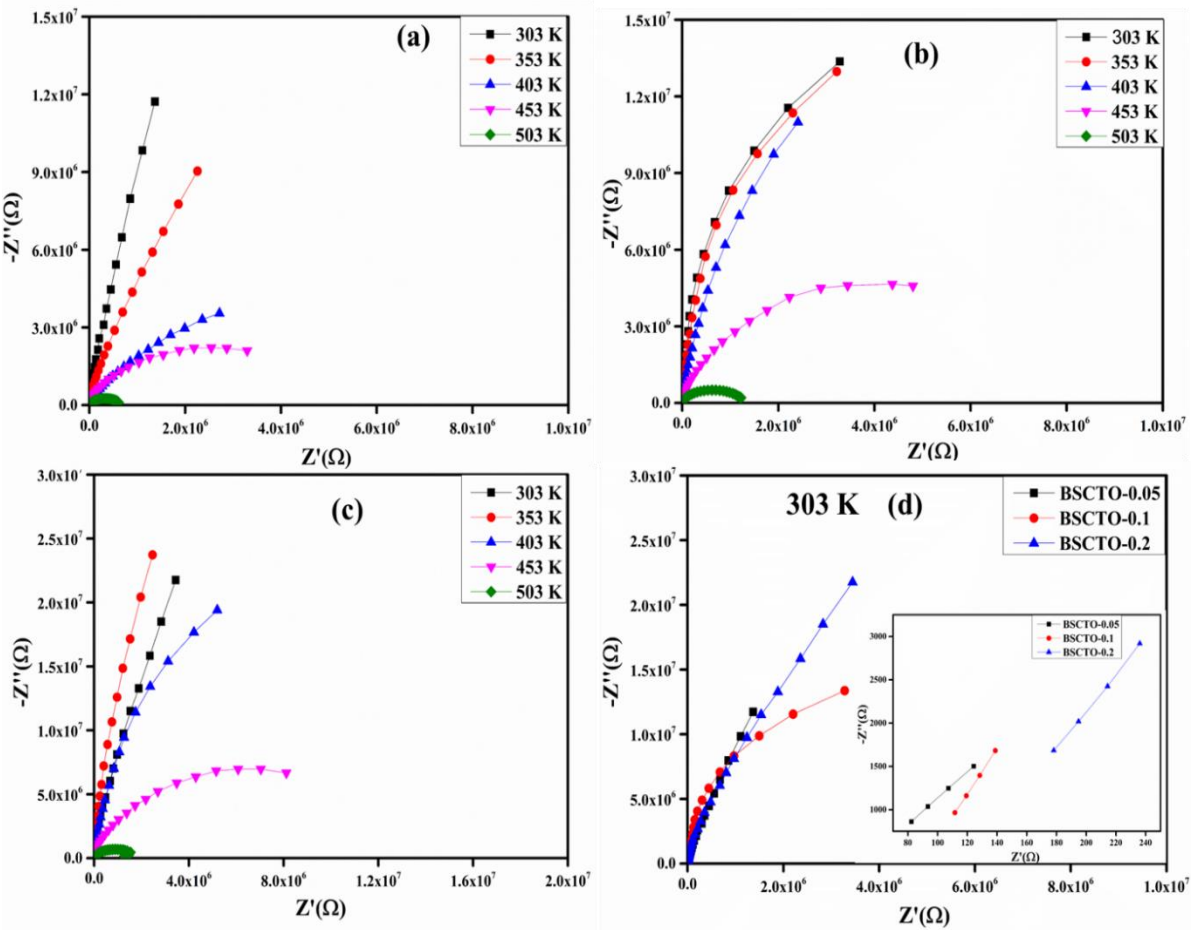

Fig. 4.9 (a-c) Complex impedance plane at different temperatures and (d) at 303 K for BSCTO-0.05, BSCTO-0.1, and BSCTO-0.2 ceramics.

To comprehend the conduction mechanism, the variation of AC conductivity with temperature was assessed. Figure **4.10** (a) depicts the temperature-dependent AC conductivity at 1 kHz for three distinct concentrations (x = 0.05, 0.1, 0.2) of BSCTO ceramics. The graph indicates a noticeable rise in electrical conductivity as the temperature is elevated. The temperature dependence of ac conductivity was more pronounced at lower frequencies compared to higher frequencies, primarily attributed to the presence of a thermally activated process originating from distinct localized states within the band gap [49]. the temperature-dependence of the electrical conductivity satisfies the Arrhenius Equation, as shown in Equation [53]:

$$\sigma = \sigma_o \, exp\left(\frac{-E_a}{k_B T}\right) \qquad 4.4$$

where σ_o, E_a, k_B and T denote the pre-exponential term, the activation energy of the material, the Boltzmann constant and absolute temperature, respectively. Furthermore, the graph illustrates a decrease in sample conductivity as the concentration of Sm^{3+} increases. At lower temperatures, ac conductivity remains relatively unaffected by temperature across all three samples. However, as the temperature rises, ac conductivity becomes temperature-dependent. The values of E_a for the Sm-doped BCTO samples at different concentrations (x= 0.05, 0.10, and 0.20) were calculated from the slope of plots of ln σ_{ac} vs. 1000/T, and found to be 0.48, 0.56, and 0.68, respectively. The findings reveal a concentration-dependent nature of the activation energy in BSCTO ceramics, which diminishes as the doping concentration of Sm increases. This suggests that there is an increase in the barrier height at the grain boundaries, leading to the reduction in the conductivity of the materials and consequently lowering the oxygen vacancies in the samples during the sintering process [**51**]. This demonstrates that

considerably improved E_a and resistance of the samples lead to the downfall of the electrical conductivity, dielectric loss, and accumulates space charge at the grain boundaries [**52**].

Figure **4.10** (b) depicts the frequency dependency alternating current conductivity (ac) of the various BSCTO samples studied, which was measured at RT in the frequency range 20 Hz-10 MHz. The total conductivity at a given temperature across a large frequency range can be calculated using Jonscher's power law [**56**]:

$$\sigma = \sigma_{dc} + \sigma_{ac}(\omega) = \sigma_{dc} + \alpha\omega^{n} \qquad 4.5$$

Where α symbolizes the pre-exponential factor that varies with temperature, while ω stands for the measurement frequency. The parameter n (where $n \leq 1$) signifies a temperature and material-sensitive frequency exponent, reflecting the strength of the interaction between mobile ions and the surrounding lattice. The values of n for BSCTO ceramics are obtained from the slope of the ln σ_{ac} vs ln ω curves and are 0.541, 0.576, and 0.585, respectively. It is observed that the value of exponent parameter obtained by linear square fitting increases with increasing Sm^{3+} concentration and follows opposite trends of the conductivity. As illustrated in Figure **4.10** (b), the σ_{ac} values for all examined samples in this current study exhibit a near-linear growth as the frequency rises. This observation suggests that the ceramics exhibit conduction through a hopping mechanism [**54**]. Furthermore, the concentration-dependence ac conductivity variant was detected, which may be related to trapped charges such as impurity ions and vacancies [**55**].

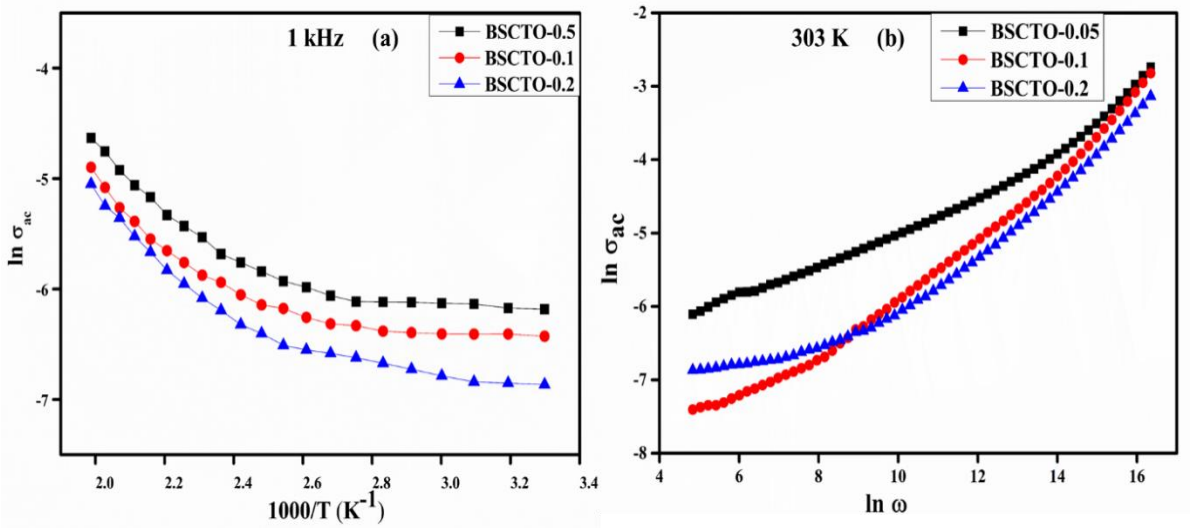

Fig. 4.10 (a) Plots of ac conductivity with temperature (1000/T) and (b) ac conductivity with angular frequency for $Bi_{(2/3)-x}Sm_xCu_3Ti_4O_{12}$ (x = 0.05, 0.10, and 0.20).

4.4. Conclusion

Finally, pure phase $Bi_{(2/3)-x}Sm_xCu_3Ti_4O_{12}$ (x = 0.05, 0.10, and 0.20) ceramics were made using the semi wet technique. According to our Rietveld refinement, the crystal structures of these ceramics have a bcc structure within the Im-3 space group. SEM micrographs demonstrated that the grain size of BCTO doped with Sm^{3+} tended to decrease, and EDX examination validated the elemental composition of the ceramics. The X-ray photoelectron spectroscopy (XPS) affirms the effective integration of Sm^{3+} in BSCTO ceramic. The dielectric constant and tan were observed to decrease with increasing Samarium concentration. At 303 K and 1 kHz, the BSCTO ceramic with higher concentrations achieved an ε' of ≈80 and a very low tan δ of 0.04. Our findings indicate that Sm doping can be used to reduce the dielectric loss of BCTO at high frequencies. Furthermore, due to their low dielectric loss and high dielectric constant, Sm-doped BCTO ceramics appear to be a good candidate for high capacitance density applications at high frequencies. The complex impedance analysis indicates that grain boundary resistances elevate with Sm-doping. The temperature-dependent conductivity

variation observed in BSCTO ceramics supports the Arrhenius law within the 303−503 K temperature range. Additionally, the alternating current (ac) conductivity of BSCTO ceramics exhibits a growth pattern as the frequency rises, consistent with Johncher's power law

4.5. References

[1] L. Liu, S. Ren, J. Liu, F. Han, J. Zhang, B. Peng, D. Wang, A. A. Bokov, Z. G. Ye, "Localized polarons and conductive charge carriers: understanding $CaCu_3Ti_4O_{12}$ over a broad temperature range," Physical Review B, **99** (2019) 094110.

[2] S. DeAlmeidaDidry, M. M. Nomel, C. Autret, C. Honstettre, A. Lucas, F. Pacreau, F. Gervais, "Control of grain boundary in alumina doped CCTO showing colossal permittivity by core-shell approach," Journal of the European Ceramic Society, 38 (2018) 3182-3187.

[3] X. Guo, Y. Pu, W. Wang, J. Ji, J. Li, M. Yang, R. Shi, "Defect chemistry and colossal dielectric behavior of Nd-modified $SrTiO_3$ lead-free ceramic materials," Ceramics International, **46** (2020) 16644-16652.

[4] J. Yuan, Y.-H. Lin, H. Lu, B. Cheng, C.-W. Nan, "Dielectric and varistor behavior of $CaCu_3Ti_4O_{12}$–$MgTiO_3$ composite ceramics," Journal of the American Ceramic Society, **94** (2011) 1966-1969.

[5] T. Li, K. Fang, J. Hao, Y. Xue, Z. Chen, "The effect of Ca-rich on the electric properties of $Ca_{1+x}Cu_{3-x}Ti_4O_{12}$ polycrystalline system," Materials Science and Engineering: B, **176** (2011) 171-176.

[6] J. L. He, F. C. Luo, J. Hu, "Cu segregation and its effects on the electrical properties of calcium copper titanate," Science China Technological Sciences, **54** (2011) 2506-2510.

[7] P. Thongbai, T. Yamwong, S. Maensiri, V. Amornkitbamrung, P. Chindaprasit, "Improved dielectric and nonlinear electrical properties of fine-grained $CaCu_3Ti_4O_{12}$

ceramics prepared by a glycine-nitrate process," Journal of the American Ceramic Society **97** (2014) 1785-1790.

[8] P. Mao, G. Lu, Q. Yan, A. Annadi, Y. Guo, Z. Wang, Z. Liu, B. Xie, L. Zhang, "Electrodes influence on the characterization of the electrical properties of colossal permittivity $CaCu_3Ti_4O_{12}$ ceramics," Ceramics International, **48** (2022) 32156-32163.

[9] N. T. Taylor, F. H. Davies, S. G. Davies, C. J. Price, S. P. Hepplestone, "The fundamental mechanism behind colossal permittivity in oxides," Advanced Materials, 31 (2019) 1904746.

[10] Y. Guo, J. Tan, J. Zhao, "Influence of CTO additives on microstructure and electrical properties of CCTO ceramics," Materials Chemistry and Physics, **278** (2022) 125659.

[11] P. Mao, C. Zeng, Y. Guo, G. Lu, Q. Yan, Z. Liu, B. Xie, Y. Zhao, K. Guo, L. Zhang, "Tuning electrical heterogeneity in $CaCu_3Ti_4O_{12}$-ZnO ceramics for high dielectric and nonlinear properties," Materials Research Bulletin, **164** (2023) 112276.

[12] P. Mao, J. Wang, S. Liu, L. Zhang, Y. Zhao, L. He, "Grain size effect on the dielectric and non-ohmic properties of $CaCu_3Ti_4O_{12}$ ceramics prepared by the sol-gel process," Journal of Alloys and Compounds, **778** (2019) 625-632.

[13] A. Rani, N. Ahlawat, R. S. Kundu, K. Rani, "Investigation of microstructural evolution and suitable potential barrier model for non-linear electrical response of Sr and Nb co-doped $CaCu_3Ti_4O_{12}$ ceramics," Physica B: Condensed Matter, **633** (2022) 413715.

[14] P. Mao, J. Wang, L. He, L. Zhang, A. Annadi, F. Kang, Q. Sun, Z. Wang, H. Gong, "Electrodes influence on the characterization of the electrical properties of colossal permittivity $CaCu_3Ti_4O_{12}$ ceramics," Ceramics International, **48** (2022) 32156-32163.

[15] T. B. Adams, D. C. Sinclair, A. R. West, "Characterization of grain boundary impedances in fine-and coarse-grained $CaCu_3Ti_4O_{12}$ ceramics," Physical review B, **73** (2006) 094124.

[16] Y. Q. Tan, J. L. Zhang, W. T. Hao, G. Chen, W. B. Su, D. L. Wang, "Giant dielectric-permittivity property and relevant mechanism of $Bi_{2/3}Cu_3Ti_4O_{12}$ ceramics," Materials Chemistry and Physics, **124** (2010) 1100-1104.

[17] L. Yang, G. Huang, T. Wang, H. Hao, Y. Tian, "Colossal dielectric permittivity and relevant mechanism of $Bi_{2/3}Cu_3Ti_4O_{12}$ ceramics," Ceramics International, **42** (2016) 9935-9939.

[18] P. Gautam, S. S. Yadava, A. Khare, K. D. Mandal, "Dielectric and magnetic studies of $0.5Bi_{2/3}Cu_3Ti_4O_{12}$-$0.5Bi_3LaTi_3O_{12}$ nano-composite ceramic synthesized by semi-wet route," Ceramics International, **43** (2017) 3133-3139.

[19] P. Gautam, A. Khare, S. Sharma, N. B. Singh, K. D. Mandal, "Characterization of $Bi_{2/3}Cu_3Ti_4O_{12}$ ceramics synthesized by semi-wet route," Progress in Natural Science: Materials International, **26** (2016) 567-571.

[20] D. Prajapati, V. S. Rai, V. Kumar, M. K. Verma, A. Kumar, N. B. Singh, K. D. Mandal, "Investigation on the effect of Dy doping on the microstructure, dielectric, electrical, and magnetic properties of $Bi_{2/3}Cu_3Ti_4O_{12}$ ceramic," Journal of Materials Science: Materials in Electronics, **34** (2023) 634.

[21] V. S. Rai, D. Prajapati, M. K. Verma, V. Kumar, S. Pandey, T. Das, N. B. Singh, K. D. Mandal, "Influence of Zn doping on microstructure, dielectric, and electric properties in $Bi_{2/3}Cu_3Ti_4O_{12}$ ceramic synthesized by the semi-wet method," Journal of Materials Science: Materials in Electronics, **33** (2022) 14868-14881.

[22] V. S. Rai, S. Pandey, V. Kumar, M. K. Verma, A. Kumar, S. Singh, D. Prajapati, K. D. Mandal, "Investigation of microstructure and dielectric behavior of $Bi_{2/3}Cu_{3-x}Mg_xTi_4O_{12}$ (x= 0, 0.05, 0.1 and 0.2) ceramics synthesized by semi-wet route," Journal of Materials Science: Materials in Electronics, **32** (2021) 7671-7680.

[23] Z. Peng, P. Liang, X. Wang, H. Peng, X. Chen, Z. Yang, X. Chao, "Fabrication and characterization of $CdCu_3Ti_4O_{12}$ ceramics with colossal permittivity and low dielectric loss," Materials Letters, **210** (2018) 301-304.

[24] M. T. Kebede, V. Dillu, S. Devi, S. Chauhan, "Phase transition and optical properties of samarium-doped $BiFeO_3$ nanoparticles," Journal of Materials Science: Materials in Electronics, **31** (2020) 19950-19960.

[25] M. Basak, M. L. Rahman, M. F. Ahmed, B. Biswas, N. Sharmin, "The use of X-ray diffraction peak profile analysis to determine the structural parameters of cobalt ferrite nanoparticles using Debye-Scherrer, Williamson-Hall, Halder-Wagner and Size-strain plot: Different precipitating agent approach," Journal of Alloys and Compounds, **895** (2022) 162694.

[26] C. Anthonyraj, M. Muneeswaran, S. GokulRaj, N. V. Giridharan, V. Sivakumar, G. Senguttuvan, "Effect of samarium doping on the structural, optical and magnetic properties of sol–gel processed $BiFeO_3$ thin films," Journal of Materials Science: Materials in Electronics, **26** (2015) 49-58.

[27] X. Zhai, H. Deng, W. Zhou, P. Yang, J. Chu, "Strain-induced structural phase transition, ferromagnetic and optical properties of $Bi_{1-x}Tb_xFeO_3$ thin films," Journal of Physics D: Applied Physics, **48** (2015) 385002.

[28] M. Zhong, N. P. Kumar, E. Sagar, Z. Jian, H. Yemin, P. V. Reddy, "Structural, magnetic and dielectric properties of Y doped $BiFeO_3$," Materials Chemistry and Physics, **173** (2016) 126-131.

[29] H. Singh, K. L. Yadav, "Structural, dielectric, vibrational and magnetic properties of Sm doped $BiFeO_3$ multiferroic ceramics prepared by a rapid liquid phase sintering method," Ceramics International, **41** (2015) 9285-9295.

[30] A. D. Sharma, H. B. Sharma, "Structural, optical, and dispersive parameters of (Gd, Mn) co-doped $BiFeO_3$ thin film," Materials Today: Proceedings, **65** (2022) 2837-2843.

[31] R. R. Awasthi, B. Das, "Structural transition and tunable optical, morphological and magnetic properties of Mn-doped $BiFeO_3$ films," Optik, **194** (2019) 162973.

[32] Z. D. Li, L. Cheng, S. L. Zhang, Z. H. Wang, C. L. Fu, "Enhanced photocatalytic and magnetic recovery performance of Co-doped $BiFeO_3$ based on MOFs precursor," Journal of Solid State Chemistry, **279** (2019) 120978.

[33] M. Wang, M. Y. You, P. Y. Guo, H. Y. Tang, C. M. Lv, Y. Zhan, T. Zhu, J. Han, "Hydrothermal synthesis of Sm-doped Bi_2MoO_6 and its high photocatalytic performance for the degradation of Rhodamine B," Journal of Alloys and Compounds, **728** (2017) 739-746.

[34] Z. Li, J. Wu, W. Wu, "Composition dependence of colossal permittivity in $(Sm_{0.5}Ta_{0.5})_xTi_{1-x}O_2$ ceramics," Journal of Materials Chemistry C, 3 (2015) 9206-9216.

[35] V. Kumar, S. Pandey, A. Kumar, M. K. Verma, S. Singh, V. S. Rai, D. Prajapati, T. Das, A. Sharma, C. L. Prajapat, A. Gangwar, "Investigation of dielectric, magnetic and impedance spectroscopic properties of $CaCu_{3-X}Mn_XTi_{4-X}Mn_XO_{12}$ (X= 0.10) nano-

ceramic synthesized through semi-wet route," Journal of Materials Research and Technology, **9** (2020) 12936-12945.

[36] C. Tian, Q. Yao, Z. Tong, H. Zhou, G. Rao, J. Deng, Z. Wang, J. Wang, "Effects of Sm-doping on microstructure, magnetic and microwave absorption properties of BiFeO3," Journal of Rare Earths, **39** (2021) 835-843.

[37] S. Kawrani, M. Boulos, D. Cornu, M. Bechelany, "From synthesis to applications: copper calcium titanate (CCTO) and its magnetic and photocatalytic properties," Chemistry Open, **8** (2019) 922-950.

[38] A. Z. Simões, L. S. Cavalcante, F. Moura, E. Longo, J. A. Varela, "Structure, ferroelectric/magnetoelectric properties and leakage current density of $(Bi_{0.85}Nd_{0.15})FeO_3$ thin films," Journal of alloys and compounds, **509** (2011) 5326-5335.

[39] P. Thongbai, B. Putasaeng, T. Yamwong, S. Maensiri, "Modified giant dielectric properties of samarium doped $CaCu_3Ti_4O_{12}$ ceramics," Materials Research Bulletin, **47** (2012) 2257-2263.

[40] H. Lin, W. Xu, H. Zhang, C. Chen, Y. Zhou, Z. Yi, "Origin of high dielectric performance in fine grain-sized $CaCu_3Ti_4O_{12}$ materials," Journal of the European Ceramic Society **40** (2020) 1957-1966.

[41] I. Jalafi, A. Bendahhou, K. Chourti, F. Chaou, S. E. Barkany, M. Abou-Salama, "High permittivity and low dielectric loss of the $(Ca_{0.9}Sr_{0.1})_{1-x}La_{2x/3}Cu_3Ti_4O_{12}$ ceramics," Ceramics International **49** (2023) 10213-10223.

[42] M. S. Alkathy, K. K. Bokinala, K. C. James Raju, "Effect of Li and Bi co-substituted on structural and physical properties of $BaTiO_3$ ceramics," Journal of Materials Science: Materials in Electronics, **27** (2016) 3175-3181.

[43] D. Panda, S. S. Hota, R. N. P. Choudhary, "A brownmillerite electronic material $LiBiFe_2O_5$: structural, dielectric, electrical, and ferroelectric properties for device application," Phase Transitions, **96** (2023) 822-839.

[44] S. Singh, A. Kaur, P. Kaur, L. Singh, "High-temperature dielectric relaxation and electric conduction mechanisms in a $LaCoO_3$-modified $Na_{0.5}Bi_{0.5}TiO_3$ system," ACS omega, **8** (2023) 25623-25638.

[45] L. Tang, F. Xue, P. Guo, Z. Luo, Z. Xin, W. Li, "Vanadium doping for lowering the preparation temperatures of $CaCu_3Ti_4O_{12}$ ceramics and its effect on their microstructures and dielectric properties," Journal of Materials Science: Materials in Electronics, **29** (2018) 9435-9441.

[46] J. Wang, Z. Lu, T. Deng, C. Zhong, Z. Chen, "Improved dielectric properties in A′-site nickel-doped $CaCu_3Ti_4O_{12}$ ceramics," Journal of the American Ceramic Society, **100** (2017) 4021-4032.

[47] G. Du, F. Wei, W. Li, N. Chen, "Co-doping effects of A-site Y^{3+} and B-site Al^{3+} on the microstructures and dielectric properties of $CaCu_3Ti_4O_{12}$ ceramics," Journal of the European Ceramic Society, **37** (2017) 4653-4659.

[48] B. K. Paul, D. Mondal, D. Bhattacharya, S. Datta, M. Kundu, I. Mondal, P. Halder, S. Sarkar, A. Ghosh, T. K. Mandal, S. Das, "Transition metal impregnated nanostructured oxide material for broadband electromagnetic interference shielding: A theoretical and experimental insight," Chemical Engineering Journal, **459** (2023) 141560.

[49] Y. Slimani, A. Selmi, E. Hannachi, M. A. Almessiere, A. Baykal, I. Ercan, "Impact of ZnO addition on structural, morphological, optical, dielectric and electrical

performances of $BaTiO_3$ ceramics," Journal of Materials Science: Materials in Electronics, **30** (2019) 9520-9530.

[50] P. Saengvong, J. Boonlakhorn, J. Jumpatam, N. Chanlek, J. Prasongkit, B. Putasaeng, P. Moontragoon, P. Srepusharawoot, P. Thongbai, "Effects of sintering condition on giant dielectric and nonlinear current-voltage properties of $Na_{1/2}Y_{1/2}Cu_3Ti_{3.975}Ta_{0.025}O_{12}$ ceramics," Heliyon, **9** (2023).

[51] M. Li, Q. Liu, C. X. Li, "Study of the dielectric responses of Eu-doped $CaCu_3Ti_4O_{12}$," Journal of Alloys and Compounds, 699 (2017) 278-282.

[52] I. Coondoo, A. K. Jha, S. K. Agarwal, "Enhancement of dielectric characteristics in donor doped Aurivillius $SrBi_2Ta_2O_9$ ferroelectric ceramics," Journal of the European Ceramic Society, **27** (2007) 253-260.

[53] M. A. Mosa, M. K. Das, F. Alam, "Enhanced multiferroic properties in Ba and Sm co-doped $BiFeO_3$ ceramics," Journal of Materials Science: Materials in Electronics, **33** (2022) 25089-25102.

[54] W. B. Taazayet, I. M. Zouari, B. Dkhil, N. T. Mliki, "Optical and dielectric properties of ultra-fine Mn doped $BiFeO_3$ nanoparticles," Inorganic Chemistry Communications, **154** (2023) 110951.

[55] Peng, P. Liang, J. Wang, X. Zhou, J. Zhu, X. Chao, Z. Yang, "Interfacial effect inducing thermal stability and dielectric response in $CdCu_3Ti_4O_{12}$ ceramics," Solid State Ionics, **348** (2020) 115290.

[56] S. Pandey, V. Kumar, K. D. Mandal, "Studies of sintering temperature on the microstructure, magnetic and dielectric behavior of $CaCu_3Ti_{3.5}Mn_{0.5}O_{12}$ ceramic synthesized by semi-wet route," SN Applied Sciences, **2** (2020) 1-9.